TOWARDS CARTILAGE DIAGNOSIS IN X-RAY PHASE-CONTRAST INTERFEROMETRY

J. Bopp[⋆], *P. Bartl*[‡], *L. Ritschl*[‡], *M. Radicke*[‡], *A. Maier*[⋆], *G. Anton*[†], *C. Riess*[⋆]

[⋆]Pattern Recognition Lab, Department of Computer Science,
Friedrich-Alexander-Universität Erlangen-Nürnberg, Erlangen, Germany
[†]Erlangen Centre for Astroparticle Physics (ECAP),
Friedrich-Alexander-Universität Erlangen-Nürnberg, Erlangen, Germany
[‡] Siemens Healthcare GmbH, Erlangen, Germany

ABSTRACT

Osteoarthritis is a common cartilage disease, particularly in societies with aging population. Over 80% of the people over 75 years are affected in the USA. MRI and X-ray can be used to image cartilage, but both approaches suffer from specific drawbacks. X-ray Talbot-Lau interferometers (TLI) have the potential to unite benefits from both modalities. However, TLI setups require to be carefully designed for an imaging task, and the design process itself is not yet well understood.

In this paper, we present an optimization framework for directly visualizing cartilage in the knee with phase-contrast imaging. First, we create simulated phantoms and make a setup-independent choice for an X-ray spectrum that maximizes the theoretically possible contrast to noise ratio over dose. Then, we analytically adapt a Talbot-Lau interferometer to the best spectrum for a knee phantom. It turns out that cartilage can be visualized with an effective dose of 1.16 mSv.

Index Terms— Optimization method, Tissue, X-ray imaging

1. INTRODUCTION

Cartilage damages are one of the most common injuries. They can be caused by different reasons, for example in accidents or as a result of long-term stress of the body part. One typical disease is osteoarthritis, causing a degeneration of the cartilage inside a joint. In the US, osteoarthritis is second as a cause of work disability, more than 50% of the population over 65 years is affected, and even 80% over 75 years [1].

The current gold standard for diagnosing osteoarthritis is magnetic resonance imaging (MRI), due to its ability to directly visualize cartilage. An alternative to MRI is X-ray with a contrast agent [2]. X-ray allows to image the patient in standing (weight-bearing) conditions [3, 4], which is not possible in MRI. Although any X-ray imaging technique also deposits dose in the patient, X-ray weight-bearing scans indirectly visualizes cartilage in a symptomatic state, and hence open new diagnostic opportunities for osteoarthritis. However, contrast agent has to be injected into the joint capsule, since the X-ray soft-tissue contrast is insufficient to image cartilage directly. Figure 1 shows a knee joint of the right leg in anterior view. The interesting cartilage is marked in blue for the lateral condyle and in violet the medial condyle both coated with articular cartilage.

Thanks to Siemens Healthenieers for funding. The concepts and information presented in this paper are based on research and are not commercially available.

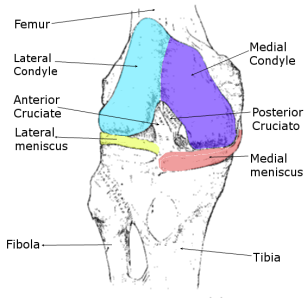

Fig. 1. Right knee-joint in anterior view. Cartilage of interest is highlighted: lateral condyle (light blue) and the medial condyle (violet) both with articular cartilage. Lateral meniscus (yellow) and medial meniscus (red) with the underlying articular cartilage.

In yellow, and red the two menisci with the articular cartilage underneath. Osteoarthritis can be diagnosed by measuring the thickness of the cartilage. However, the use of contrast agent can have adversarial side effects. First, contrast agents bears a risk on its own, especially for people with renal insufficiency, allergies, or intolerances. Furthermore, the invasive nature of contrast agents generally reduces its acceptance by the patients. Thus, the long-term goal of this work is to create an interferometric X-ray imaging system for imaging cartilage under weight-bearing conditions without contrast agents at a clinically acceptable patient dose. As a first step towards this goal, we study the fundamental feasibility of this approach, identify key parameters for the system design, and provide an upper bound on the expected patient dose for such a setup based on a simulation under realistic assumptions. The resulting system can potentially also be used for diagnosing other cartilage diseases.

We use the grating-based Talbot-Lau interferometer (TLI) to acquire phase-contrast X-ray images, for several reasons. A TLI can be mounted to traditional clinical X-ray systems, while providing overall good soft-tissue contrast. TLI provides standard X-ray attenuation plus complementary information on the differential phase shift and the dark-field [5, 6]. The latter reveals structure variations at (sub-)micron scale [7]. Compared to MRI, Talbot-Lau interferometers can provide three benefits. First, a shorter scanning time, which is highly important in a scanning protocol where the patient is standing in a discomforting position. A large degree of freedom in designing almost arbitrary weight bearing tasks as well as a cost criterion. The advantages towards direct radiography are the additional phase-contrast image which is able to directly visualize the cartilage

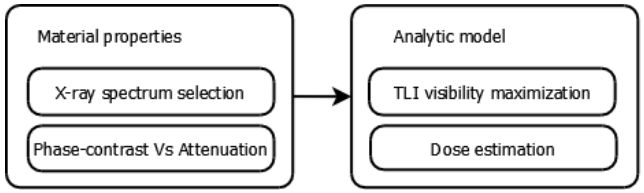

Fig. 2. The two parts of our optimization framework. We first derive constraints from material properties of cartilage and water (left). Then, we add setup-specific constraints to optimize a Talbot-Lau interferometer for cartilage imaging and estimate patient dose (right).

and the use of contrast agent can be avoided. Stutman *et al.* showed that a differentiation between water, bone, and cartilage is in principle possible with an interferometric setup [8]. However, the overall tradeoffs between patient dose, setup geometry, spectra, and image contrast are currently not yet well understood.

Towards the goal of phase-sensitive cartilage imaging, we present a set of ideas for task-based TLI setup optimization. First, we validate that cartilage contrast is considerably higher when looking at phase rather than at absorption. Second, we use these material properties to seek the best X-ray spectrum for cartilage visualization. Then, we adapt and optimize an existing TLI setup to that spectrum and the cartilage imaging task. Dose computations for this setup show that directly visualizing cartilage may be very well possible at a clinically acceptable dose.

2. METHODS

The design space for a phase-sensitive cartilage imaging system is potentially huge. We approach this problem by making a series of decisions that increasingly narrow down the degrees of freedom for system design. A sketch of our workflow is shown in Fig. 2. The first steps towards optimizing the setup are performed in the left part, by deriving fundamental boundaries from the material properties of cartilage and water. This is described in Sec. 2.1. In the right part, described in Sec. 2.2, we use these boundaries to constrain an actual Talbot-Lau interferometer, and introduce additional realistic constraints to narrow down the design space. Using a link between the system sensitivity and the required dose, it becomes possible to estimate the expected patient dose for cartilage imaging using a Talbot-Lau interferometer.

2.1. Material Properties

We create numerical phantoms to study the fundamental properties of water/cartilage interfaces. Each phantom consists of a water cylinder with embedded cartilage. The cylinder diameter ranges from 2 cm to 20 cm to simulate different body parts like fingers, wrists, and knees. Each cylinder contains a 5 mm water-cartilage interface to model cartilage surrounded by joint fluid.

The energy-dependent complex refractive index $\eta_m = 1 - \delta_m + i\beta_m$ characterizes in δ the phase shift and in β the absorption of a material [9, p. 61]. We compute the refractive indices of water η_{water} and cartilage $\eta_{\mathrm{cartilage}}$ using tabulated values[1].

[1]For η_{water}, we use 11.2 % H and 88.8 % O (percentages by mass) with a density of $\rho_{\mathrm{water}} = 0.998\ \frac{\mathrm{g}}{\mathrm{cm}^3}$. For $\eta_{\mathrm{cartilage}}$, we use 9.6% H, 9.9% C, 2.2% N, 74.4% O, 0.5% Na, 2.2% P, 0.9% S and 0.3% Cl (percentages by mass) with a density of $\rho_{\mathrm{cartilage}} = 1.1\ \frac{\mathrm{g}}{\mathrm{cm}^3}$ [10]

The total refractive angle of a homogeneous material m is determined by its phase shift Φ,

$$\Phi_m(\lambda) = 2 \cdot \pi \frac{\delta_m(\lambda)}{\lambda} \Delta z \ . \tag{1}$$

Here, λ denotes the wavelength and Δz the spatial extent of the material in direction of the wave propagation.

2.1.1. Phase-Contrast vs. Attenuation

An important question is the potential benefits of phase-contrast imaging over attenuation imaging. For comparison the contrast to noise ration over dose (CNRD) is compared for the phase δ and the attenuation β. These CNRD values are a fundamental upper bound on the achievable contrast, independent of any concrete implementation of a phase-sensitive imaging system. This is done for four different spectra with 30 kVp, 40 kVp, 50 kVp, and 60 kVp, each with a 0.3 mm copper filter. The spectra were simulated with [11, 12]. The potential benefit b of phase imaging will be calculated by

$$b = \frac{\mathrm{CNRD}^{\delta}}{\mathrm{CNRD}^{\beta}} \ . \tag{2}$$

To get the CNRD^{δ}, we first calculate the phase shift by

$$\mathrm{S}^{\delta}_m(\lambda) = \int_{z=0}^{Z} \delta_m(\lambda)\, dz \ , \tag{3}$$

which are line integrals of the energy-dependent δ_m in a homogeneous material m in propagation direction z. CNRD^{δ} is computed as

$$\mathrm{CNRD}^{\delta} = \int_{\lambda} \frac{\mathrm{S}^{\delta}_{\mathrm{cartilage}}(\lambda) - \mathrm{S}^{\delta}_{\mathrm{water}}(\lambda)}{\sqrt{n(\lambda)} \cdot \mathrm{att}(\mathrm{water}, \lambda) \cdot n(\lambda) \cdot \frac{\mathrm{hc}}{\lambda}}\, d\lambda \ , \tag{4}$$

where $n(\lambda)$ denotes the relative occurrence of photons of wavelength λ in the spectrum, $\mathrm{att}(\mathrm{water}, \lambda)$) denotes the attenuation of water, and h and c denote Planck's constant and the speed of light, respectively. The contrast is computed in the numerator of Eqn. 4. In the denominator, the noise is modeled as the square root of the number of photons $n(\lambda)$, and dose is modeled by the remaining factors as the absorbed energy in water. CNRD^{β} can be calculated analogously by replacing δ by β in Eqn. 3 and Eqn. 4.

2.1.2. Spectrum Selection for CNRD Maximization

The CNRD approach for comparing the phase shift with the attenuation can be slightly modified to relate the theoretically obtainable CNRD for different X-ray spectra. The best spectrum for visualizing the phase shift is selected. Therefore, the contrast to noise ratio over dose (CNRD) is computed for distinguishing cartilage and water by the real part of their complex refractive index δ. We compare the four different spectra to evaluate the highest CNRD^{δ} for the different phantoms.

2.2. Analytic model

In this project we focus on grating-based interferometers with three gratings in a so called Talbot-Lau interferometry (TLI) setup. One major advantage of TLI over other designs is that it can be operated with conventional non-coherent X-ray tubes, and yet provides reasonably high sensitivity [13]. In that sense, it is the setup that shows the greatest potential to be translated into clinical practice.

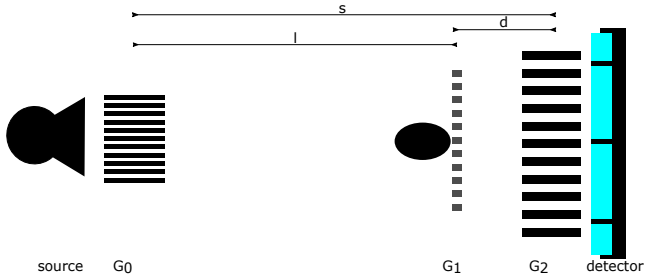

Fig. 3. TLI setup with a medical source, a source grating G_0, a phase shifting grating G_0, the analyzer grating G_2 and the detector.

A sketch of a TLI system is shown in Fig. 3. Grating G_0 splits an incoming incoherent wave into a set of individually coherent, but mutually incoherent waves. This so-called Lau effect [14] allows to use conventional medical X-ray tube. Grating G_1 imprints a phase shift pattern onto the wave front. At certain distances behind G_1, this shift leads to a sinusoidal interference pattern, also called Talbot self image [15]. Since the period of the interference pattern is much smaller than one detector pixel, grating G_2 samples the pattern at multiple, slightly shifted positions, which is called phase stepping. To obtain a phase-sensitive image, an object within the setup distorts the wave front and the intensity pattern at G_2. Under ideal conditions, any deviations from the expected interference pattern at G_2 can be attributed to the first derivative of the phase shift of the object.

Note that grating G_2 attenuates half about of the photons behind the patient. In other words, half of the photons add only to the patient dose, not to the image contrast. Consequently, the potential benefit b of CNRD$^{\delta}$ over CNRD$^{\beta}$ in Eqn. 2 has to be reduced by a factor of 2 for TLI systems [16].

An important quality metric of TLI is the visibility V. Let $\mathbf{r}$ denote the recorded phase stepping intensities of an empty scene. Then, visibility is defined as

$$V = \frac{\max(\mathbf{r}) - \min(\mathbf{r})}{\max(\mathbf{r}) + \min(\mathbf{r})} \quad . \tag{5}$$

The analytic model by Thuering and Stampanoni [17] introduces the minimally detectable refractive angle $\alpha_{\min}(\lambda)$ of a setup,

$$\alpha_{\min}(\lambda) \equiv \sigma_{\alpha}(\lambda) = \frac{p_2}{2\pi d} \frac{\sqrt{2\chi_{\det}(\lambda)}}{V(\lambda)\sqrt{n(\lambda)}} \quad . \tag{6}$$

Here, p_2 is the G_2 period, d is the distance between G_1 and G_2, $V(\lambda)$ the visibility, and $n(\lambda)$ the number of photons, and $\chi_{\det}(\lambda)$ summarizes effects of a non-ideal X-ray detector. The smaller $\alpha_{\min}(\lambda)$, the more sensitive is a phase-sensitive imaging system.

The key to relate a specific setup geometry with the required dose for an imaging task is to link $\alpha_{\min}(\lambda)$ to to the required refractive angle for cartilage/water contrast $\alpha_{\mathrm{c,w}}$,

$$\alpha_{\min}(\lambda) \leq (\mathrm{S}^{\delta}_{\mathrm{cartilage}}(\lambda) - \mathrm{S}^{\delta}_{\mathrm{water}}(\lambda))\, \Delta z = \alpha_{\mathrm{c,w}}(\lambda) \quad . \tag{7}$$

Thus, in order to obtain contrast between cartilage and water, the minimally detectable angle $\alpha_{\min}(\lambda)$ must be lower than the sample's refracted angle $\alpha_{\mathrm{c,w}}(\lambda)$. To minimize $\alpha_{\min}(\lambda)$, any of the parameters in Eqn. 6 could theoretically be tuned. In practice, however, most of the quantities in Eqn. 6 are relatively fixed: p_2 is typically chosen as wide as possible to maximize the height of G_2, which is coupled with the choice of p_2. Optimizing the detector parameters

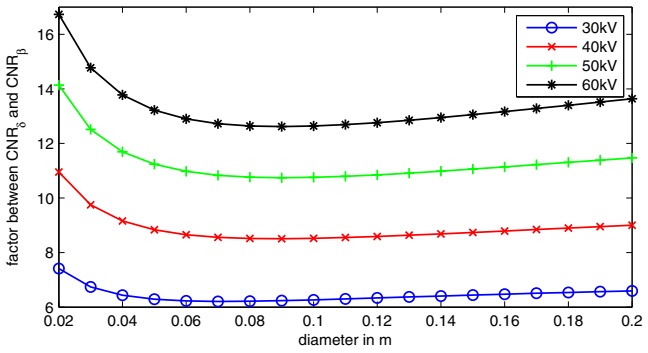

Fig. 4. Cartilage phase-shift compared to absorption regarding the possible CNRD for several polychromatic spectra. The phase shift CNRD$^{\delta}$ is about six times higher (for a 30 kVp spectrum) to about 13 times higher (for a 60 kVp spectrum).

$\chi_{\det}(\lambda)$ may not be possible in practice, particularly if the TLI system is intended to be an add-in to an existing medical X-ray system. Increasing d leads to a worse photon statistics at the detector because of the inverse square law. The two remaining parameters are visibility $V(\lambda)$ and photon counts $n(\lambda)$. Both parameters can relatively flexibly be changed, and are thus the most important parameters for lowering the minimally detectable angle $\alpha_{\min}(\lambda)$.

2.2.1. *Optimization of the Visibility to Minimize* $\alpha_{\min}$

We optimize the interferometer with the analytic simulation by investigating design energies in steps of 0.5 keV, and modifying height, period and position of grating G_1 (the remaining parameters are either consequences of these choices, or considered immutable for practical reasons).

However, the analytic model contains some optimistic simplifications that do not hold in reality. For example, grating G_1 is assumed to identically shift photons of all energies by a factor of π. To obtain a much more realistically grounded value for the polychromatic visibility, we investigated selected setup designs with a full wave propagation simulation that has been validated with actual measurements [18]. Such simulations are computationally much more expensive, but also more accurate.

2.2.2. *Necessary Effective Dose*

To calculate the minimally detectable angle $\alpha_{\min}$ for our case of polychromatic spectra, Eqn. 6 can not be used directly. However, the polychromatic $\alpha_{\min}$ can be computed by using of $\alpha_{\min}(\lambda) \equiv \sigma_{\alpha}(\lambda)$ in Eqn. 6 and the quadratic sum rule of error propagation:

$$\alpha^2_{\min} = \sum w_i^2 \alpha^2_{\min}(\lambda_i) \tag{8}$$

for all wavelengths λ_i and an energy-dependent weighting factor w_i [19, p. 41-43]. Any remaining gap between the cartilage refractive angle $\alpha_{\mathrm{c,w}}$ and $\alpha_{\min}$ must be bridged by increasing the dose. In Eqn. 6, the number of photons $n(\lambda)$ (and hence, the dose) have to be increased quadratically to linearly improve $\alpha_{\min}$. The effective deposited dose E is computed in these steps: we calculate the number of photons that are attenuated in the phantom, multiplied by the photon energy and integrated across all energies. This energy is converted to J/kg resulting in the equivalent dose absorbed by tissue

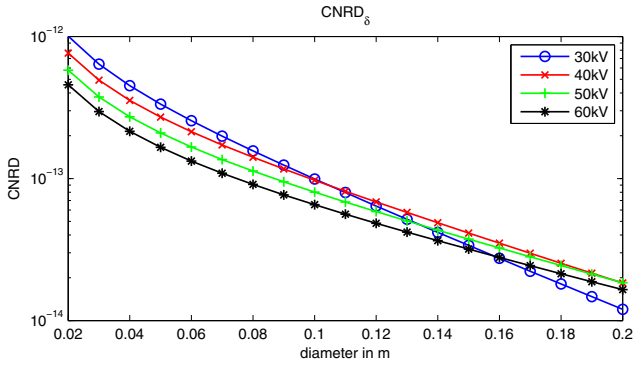

Fig. 5. Comparison between the CNRD$^{\delta}$ of the spectra on phantoms of varying diameters. The peak energy of the optimum spectrum increases with the phantom diameter, ranging from 30 kVp (below 10 cm) over 40 kVp (10 cm to 20 cm) to 50 kVp (over 20 cm).

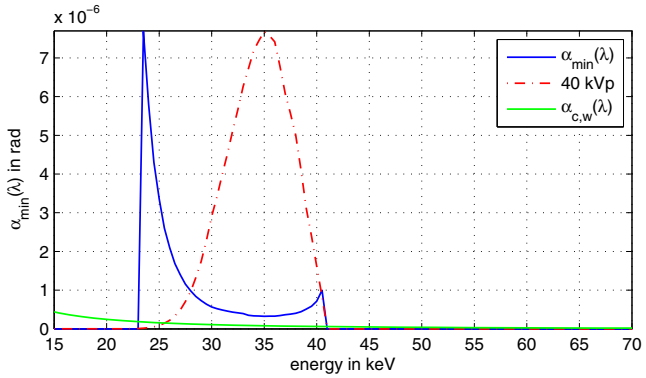

Fig. 6. Overlay of the 40 kVp spectrum (red), $\alpha_{\mathrm{min}}(\lambda)$ of the visibility-optimized system with increased dose (blue) and the required detectable refractive angle for cartilage $\alpha_{\mathrm{c,w}}(\lambda)$ (green).

h_T. Eventually, the effective dose is calculated by

$$e = \sum_T \mathrm{w}_T \cdot h_T = \sum_T \mathrm{w}_T \cdot \sum_R \mathrm{w}_R \cdot \bar{d}_{T,R} \ , \qquad (9)$$

where $\mathrm{w}_T = 0.01$ is a organ-specific parameter and w_R is a radiation weighting factor, which in our case is 1. $\bar{d}_{T,R}$ is the mass-averaged absorbed dose in tissue T by radiation type R [20].

3. RESULTS

We create phantoms consisting of water cylinders with diameters between 2 cm and 20 cm, containing a 5 mm cartilage/water interface.

The theoretically possible benefits of measuring phase shifts compared to attenuation (Eqn. 2) are visualized in Fig. 4. The X-axis shows different phantom diameters. The Y-axis shows $\frac{\mathrm{CNRD}_\delta}{\mathrm{CNRD}_\beta}$ for 30 kVp to 60 kVp spectra. The showed factors are consistently larger than 1, i.e., CNRD_δ is larger than CNRD_β. These factors can be interpreted as the safety margin for the design of a phase-sensitive system: measurement of phase may be less efficient than absorption by this factor, in order to achieve equal CNRD to absorption (for example, it is known that a Talbot-Lau interferometer loses by design a factor of at least 2, due to post-patient attenuation at grating G_2 [16]). Conversely, any increase in phase measurement efficiency translates in a gain of phase CNRD over absorption CNRD.

Figure 5 shows the CNRD$^{\delta}$ for the phase shifts at the cartilage/water interface for each of the four investigated X-ray Tungsten spectra (indicated by their peak voltages; unless explicitly stated otherwise, each spectrum is additionally filtered with 0.3 mm copper). The optimal spectrum depends on the phantom diameter. For diameters below 10 cm, a 30 kVp spectrum achieves the highest CNRD$^{\delta}$. For diameters between 10 cm and 20 cm, a 40 kVp spectrum is performs best. For diameters larger than 20 cm, a 50 kVp spectrum achieves the highest CNRD$^{\delta}$.

For cartilage in knees of 10 cm diameter, the optimal spectrum w.r.t. CNRD$^{\delta}$ is the one with 40 kVp, closely followed by 30 kVp. Thus, we used the 40 kVp spectrum as input energies for an optimized Talbot-Lau interferometer. The results in Fig. 4 indicate that the potential CNRD gain over attenuation is $8.52/2 = 4.26$ (after taking the TLI penalty factor of 2 into account). Evaluating Eqn. 7 for the 40 kVp spectrum and integrating over all λ yields a cartilage refractive angle $\alpha_{\mathrm{c,w}} = 84.78$ nrad.

To detect that refractive angle the visibility of a given setup was maximized for the spectrum. It originally was designed for a higher spectrum. With a 40 kVp spectrum the (polychromatic) visibility was at 9.04%. After optimization using the analytical model, the polychromatic visibility increased to 68.62%.

The minimally detected angles for the whole spectrum can be calculated with the input spectrum as weights and the corresponding wavelength λ in Eqn. 8 resulting in $\alpha_{\mathrm{min}} = 13.13\,\mu$rad with a deposited effective dose of 12.281 nSv. However, α_{min} is a factor of about 154.8 larger than the required cartilage refractive angle $\alpha_{\mathrm{c,w}}$. Thus, to make $\alpha_{\mathrm{c,w}}$ detectable, the dose has to be increased by a factor of $(154.8)^2 \approx 24000$, which leads to an effective dose of 0.294 mSv. Figure 6 illustrates these quantities. The minimally detectable angle is $\alpha_{\mathrm{min}}(\lambda)$ is shown in blue. The required detectable refractive angle for cartilage $\alpha_{\mathrm{c,w}}(\lambda)$ is shown in green. The relative contribution of the 40 kVp spectrum to each energy is shown in red. With the more realistic numerical simulation we obtained a visibility of 28% for the analytically best setup (which we did not further optimize at this point). Taking into consideration that the numerical simulation showed a much lower visibility of only 28%, it is very likely that the actually required dose is considerably higher. For example, if we estimate the visibility of a perfectly optimized realistic system to be half of the visibility of the analytic simulation, then the effective dose is 1.176 mSv.

4. CONCLUSIONS

The results show that cartilage diagnostics are an interesting application for phase-sensitive imaging. For cartilage, the contrast-to-noise ratio over dose is a factor higher for the phase shift than for the attenuation. We find that cartilage can be directly imaged with a Talbot-Lau Interferometer at a dose between 0.294 mSv and 1.176 mSv — which is within or very close to a clinically acceptable value of 1 mSv. Furthermore, the design space can be more thoroughly searched with full wave propagation simulations, which may lead to a tighter upper bound on the expected dose. We also plan to validate our simulations with actual cartilage measurements.

Beyond the actual application of knee imaging, we believe that our approach to task-based optimization of Talbot-Lau setups is worth reporting in its own right, and that the optimization strategy can be transferred to other imaging tasks, for example to investigate direct arthrography to avoid contrast agent.

5. REFERENCES

[1] N Arden and M C Nevitt, "Osteoarthritis: epidemiology," *Best practice & research Clinical rheumatology*, vol. 20, no. 1, pp. 3–25, 2006.

[2] H T Kokkonen, A S Aula, H Kröger, J-S Suomalainen, E Lammentausta, E Mervaala, J S Jurvelin, and J Töyräs, "Delayed computed tomography arthrography of human knee cartilage in vivo," *Cartilage*, vol. 3, no. 4, pp. 334–341, 2012.

[3] M Berger, K Müller, A Aichert, M Unberath, J Thies, J-H Choi, R Fahrig, and A Maier, "Marker-free motion correction in weight-bearing cone-beam ct of the knee joint," *Medical physics*, vol. 43, no. 3, pp. 1235–1248, 2016.

[4] E K J Tuominen, J Kankare, S K Koskinen, and K T Mattila, "Weight-bearing ct imaging of the lower extremity," *American Journal of Roentgenology*, vol. 200, no. 1, pp. 146–148, 2013.

[5] S Hu, C Riess, J Hornegger, P Fischer, F Bayer, T Weber, G Anton, and A Maier, "3d tensor reconstruction in x-ray dark-field tomography," in *Bildverarbeitung für die Medizin 2015*, pp. 492–497. Springer, 2015.

[6] A Momose, S Kawamoto, I Koyama, Y Hamaishi, K Takai, and Y Suzuki, "Demonstration of x-ray talbot interferometry," *Japanese journal of applied physics*, vol. 42, no. 7B, pp. L866, 2003.

[7] S Kaeppler, F Bayer, T Weber, A Maier, G Anton, J Hornegger, M Beckmann, P A Fasching, A Hartmann, F Heindl, et al., "Signal decomposition for x-ray dark-field imaging," in *International Conference on Medical Image Computing and Computer-Assisted Intervention*. Springer, 2014, pp. 170–177.

[8] D Stutman, T J Beck, J A Carrino, and C O Bingham, "Talbot phase-contrast x-ray imaging for the small joints of the hand," *Physics in medicine and biology*, vol. 56, no. 17, pp. 5697, 2011.

[9] D Attwood, *Soft x-rays and extreme ultraviolet radiation: principles and applications*, Cambridge university press, 2007.

[10] H Q Woodard and D R White, "The composition of body tissues," *The British journal of radiology*, vol. 59, no. 708, pp. 1209–1218, 1986.

[11] J M Boone and J A Seibert, "An accurate method for computer-generating tungsten anode x-ray spectra from 30 to 140 kv," *Medical physics*, vol. 24, no. 11, pp. 1661–1670, 1997.

[12] "Simulation of x-ray spectra," https://www.oem-products.siemens.com/x-ray-spectra-simulation Last checked: 12th Oktober 2016.

[13] F Pfeiffer, T Weitkamp, O Bunk, and C David, "Phase retrieval and differential phase-contrast imaging with low-brilliance x-ray sources," *Nature physics*, vol. 2, no. 4, pp. 258–261, 2006.

[14] J Jahns and A W Lohmann, "The lau effect (a diffraction experiment with incoherent illumination)," *Optics Communications*, vol. 28, no. 3, pp. 263–267, 1979.

[15] H F Talbot, "Lxxvi. facts relating to optical science. no. iv," *The London and Edinburgh Philosophical Magazine and Journal of Science*, vol. 9, no. 56, pp. 401–407, 1836.

[16] R Raupach and T Flohr, "Performance evaluation of x-ray differential phase contrast computed tomography (pct) with respect to medical imaging," *Medical physics*, vol. 39, no. 8, pp. 4761–4774, 2012.

[17] T Thuering and M Stampanoni, "Performance and optimization of x-ray grating interferometry," *Philosophical Transactions of the Royal Society of London A: Mathematical, Physical and Engineering Sciences*, vol. 372, no. 2010, pp. 20130027, 2014.

[18] A Ritter, P Bartl, F Bayer, K C Gödel, W Haas, T Michel, G Pelzer, J Rieger, T Weber, A Zang, et al., "Simulation framework for coherent and incoherent x-ray imaging and its application in talbot-lau dark-field imaging," *Optics express*, vol. 22, no. 19, pp. 23276–23289, 2014.

[19] P R Bevington and D K Robinson, "Data reduction and error analysis," *McGraw-Hill*, 2003.

[20] C H McCollough and B A Schueler, "Calculation of effective dose," *Medical physics*, vol. 27, no. 5, pp. 828–837, 2000.